Crack Propagation Monitoring Using an Image Deformation Approach

D. Dias-da-Costa[1,4,*], J. Valença[2], E. Júlio[2,5], H. Araújo[3]

[1]School of Civil Engineering, The University of Sydney, Sydney, NSW 2006, Australia

[2]CERIS, Instituto Superior Técnico, Universidade de Lisboa, Av. Rovisto Pais, 1049-001 Lisboa, Portugal

[3]ISR, Department of Electrical and Computer Engineering, University of Coimbra, Rua Luís Reis Santos, 3030-290 Coimbra, Portugal

[4]ISISE, Department of Civil Engineering, University of Coimbra, Rua Luís Reis Santos, 3030-290 Coimbra

[5]Department of Civil Engineering, Instituto Superior Técnico, University of Lisbon, Av. Rovisco Pais, 1049–001 Lisbon, Portugal

[*]corresponding author (daniel.diasdacosta@sydney.edu.au)

Abstract

An image deformation method is herein proposed to monitor the crack propagation in structures. The proposed approach is based on a computational algorithm that uses displacements measured by photogrammetry or image correlation to generate a virtual image of the surface, from an initial input to any given stage of analysis. This virtual image is then compared with the real image of the specimen to identify any discontinuities that appeared or evolved during the monitored period. The procedure was experimentally validated in the characterisation of crack propagation in concrete specimens. When compared with other image processing techniques, for instance based on edge detectors, the image deformation approach showed insensitiveness to any discontinuity previously existing on the surface, such as cracks, stains, voids or shadows, and did not require any specific surface treatments or lighting conditions. With this approach the global crack maps could be extracted from the surface of the structure and extremely small changes occurring within a given time interval could be characterised, such as the movement associated with the opening of cracks. It is highlighted that the proposed procedure is general and therefore applicable to detect and characterise surface discontinuities in different materials and test set-ups.

Keywords: Image Deformation Approach; Monitoring cracks; Structural health monitoring; Discontinuity detection; Photogrammetry; Digital Image Correlation.

1. Introduction

The mapping of cracks appearing at the surface of a structure is still frequently performed using a direct sketch based on visual observations, whereas the openings are evaluated by means of measuring magnifiers or crack width rulers. This rather empirical process is time-consuming and can face human errors. Fortunately, innovative technological developments have been recently brought-up to mitigate existing drawbacks [1]. Within these developments, three classes of new approaches can be identified which are based on the: i) strain field; ii) image processing; and iii) combination of both. The first approach identifies the areas of strain or curvature localisation related with cracks [2]. The strain can be calculated using the derivative of the displacement field measured by photogrammetry [3-7] and image correlation [2, 8-10], or using the electronic speckle pattern interferometry from two coherent laser beams pointed at the surface [5, 11-14]. These techniques based on the strain field are still limited to indirect characterisation of cracks.

The second approach mentioned above includes the use of image processing algorithms, such as edge detectors [15-17], transform-based methods and wavelets [18]. Most of these methods output a binarised image where any resulting discontinuities are roughly identified with a crack pattern. Unfortunately, shadows or imperfections can be wrongly identified as real cracks without a careful preparation of the surfaces and adequate lighting conditions.

More complex image processing algorithms exist which: combine mathematical morphology operations to extract linear features from the image and a modified iterative Hough transformation to detect newly formed cracks in a time interval [19]; and emulate the percolation of a fluid using brightness and shape parameters to obtain a crack map [20]. Combined approaches may allow improved results. For instance, the strain field can be used to redirect image-processing algorithms towards areas with the highest strains, i.e. areas where cracking is expected to exist [21, 22]. Nevertheless, even with this approach, there are still false detections. One possible way to mitigate this issue could be the use of neural network classifiers [23].

It has to be highlighted though that the above-mentioned procedures have been developed for detecting crack patterns at each frame regardless of any previous propagation history. For this reason, changes occurring between given time intervals, such as the movement of each side of the crack, cannot be easily identified. In addition, most techniques can only be used in simple settings and under controlled conditions (to avoid false detections).

Taking into account all the above-mentioned drawbacks, this manuscript presents an image deformation technique for structural monitoring of cracks that is computationally efficient, insensitive to false discontinuities and lighting conditions, and that can support the identification of the crack evolution within a period of time, independently of surface treatments to enhance detection.

2. Image Deformation Approach

2.1. General remarks

Consider an initial reference image frame. Given the displacement field function, $\mathbf{u}_r$, the current position of a pixel, $\mathbf{x}_c$, can be obtained from the following expression:

$$\mathbf{x}_c = \mathbf{x}_r + \mathbf{u}_r , \tag{1}$$

where $\mathbf{x}_r$ are the coordinates of the pixel in the reference frame.

The displacement field is a function of the reference position and is known for a set of discrete points using photogrammetry [3-5] or image correlation [8, 9]. A linear or nonlinear interpolation scheme is used to calculate the displacement values all over the surface [24-26]. With the displacement field function defined, Eq. (1) can be used to compute a virtual image frame for any given time instant (assumed hereafter as 'current') that predicts how the structure should look like from the initial image of the surface (see Figures 1a and 1b). If there are no new events, such as cracks forming, propagating or opening between initial and current instants, the virtual image matches the current real image from the same surface. If these events indeed occur, then they can be characterised by comparing current real and virtual frames (see Figure 1c). It is highlighted that pre-existing cracks, shadows or surface imperfections are not misleadingly identified (see Figure 1d) using this approach since they will appear in both virtual and current frames.

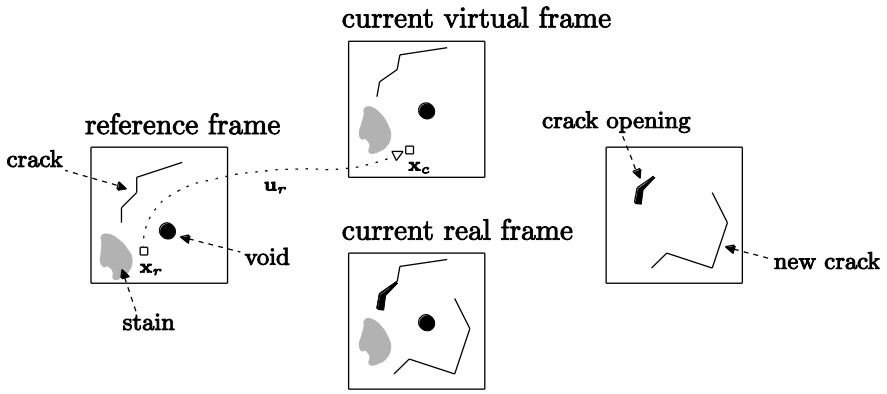

(a) (c) (d)

Figure 1 – Image deformation approach: (a) reference frame; (b) current virtual frame obtained using the displacement function and real frame; (c) current real frame; and (d) difference between current virtual and real frames.

2.2. Virtual frame computation

The virtual frame can be computed from the measured displacements using different approaches. In this section, three options are discussed.

2.2.1. Direct approach

The current virtual frame can be built directly using Eq. (1) to move all pixels in the region of interest of the reference frame to the new positions defined by the displacement field. In this case, the following drawbacks occur: i) several pixels may be moved from the reference frame into the same pixel in the virtual frame – see, for instance, pixels ‘e’ and ‘f’ in Figure 2a; and ii) unfilled pixels may appear in the virtual frame – for instance, pixels ‘d’ and ‘e’ in Figure 2a have created a gap in the virtual frame. These situations can be avoided with _a subpixel approach (see Figure 2b). The drawbacks are the minimum subpixel size required to avoid gaps and overlaps not being known beforehand, and the number of operations involved, which can become computationally demanding.

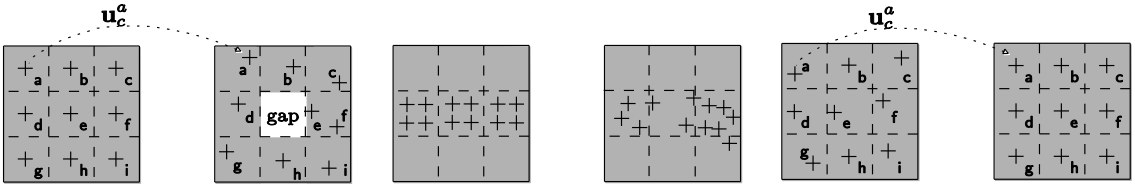

(a) (b) (c)

Figure 2 – Virtual frame computation: (a) direct pixel approach; (b) direct subpixel approach; and (c) inverse subpixel approach.

Figures 3a and 3b represents the real frame and corresponding virtual frame calculated without subpixel accuracy. It is interesting to denote that the virtual frame is almost identical to the real current frame and shows the same overall deformed shape with the exception of cracks that propagated or formed. In this way

crack patterns can easily be characterised, as it will be shown in the following sections. Figure 3c provides a magnified detail of the virtual frame where gaps are noticeable.

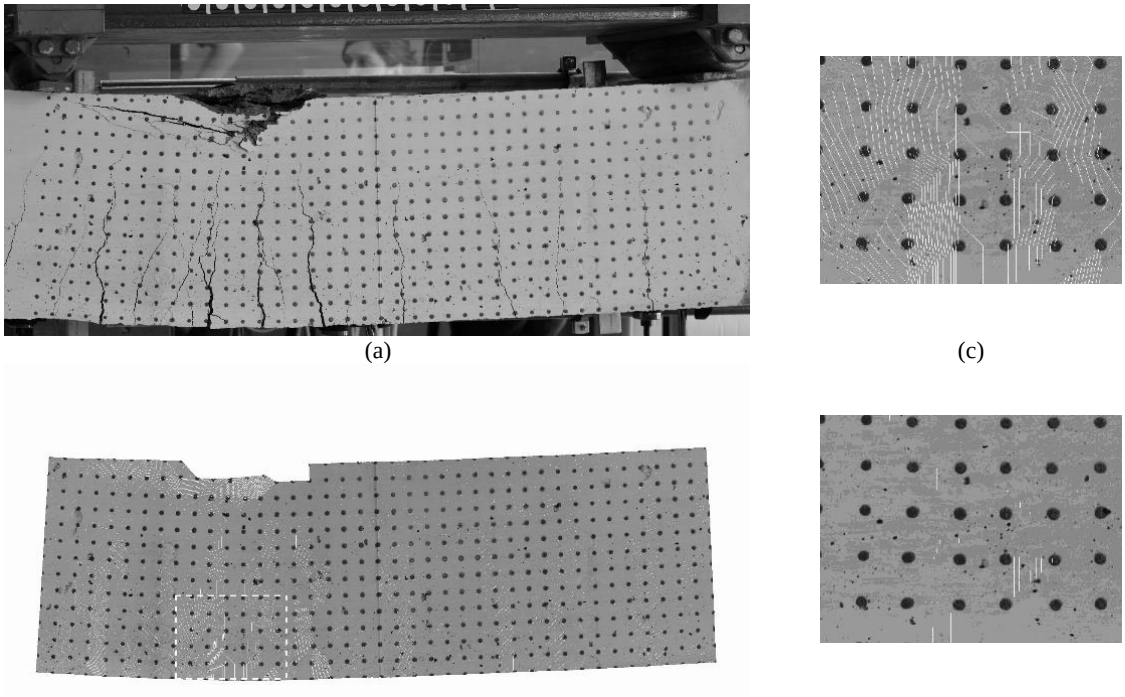

(a) (c)

(b) (d)

Figure 3 – Direct approach: (a) current real frame; (b) current virtual frame; (c) detail of the virtual frame; and (d) same detail using subpixel accuracy.

The gaps can be reduced with subpixels. For instance, in Figure 3d, each pixel is subdivided into 9 equal subdomains or subpixels, in which case the processing time grows from 1.5s to 104.8s for a region of interest of approximately 1300 x 3800 pixel. Figure 4 illustrates computing time vs. different pixel sizes.

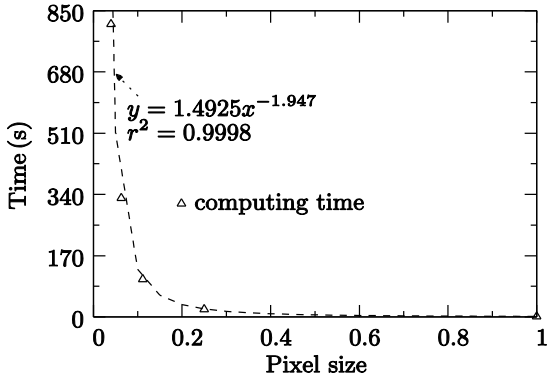

Figure 4 – Direct approach: computing time vs. pixel size.

2.2.2. Inverse approach

An inverse approach can be followed by progressively filling all pixels in the virtual image frame (Figure 2c). This requires solving a system of equations for each pixel inside the virtual frame to identify its initial position in the reference frame. This approach can be regarded as an optimised subpixel approach (compare Figures 2b and c). Accordingly, Eq. (1) can be cast in the following form:

$$\mathbf{x}_r - \mathbf{x}_c + \mathbf{u}_r\left(\mathbf{x}_r\right) = \mathbf{0} \Leftrightarrow \mathbf{F}\left(\mathbf{x}_r\right) = \mathbf{0}, \tag{2}$$

and a Newton-Raphson procedure is adopted to solve for $\mathbf{x}_r$.

If $\mathbf{x}_r^{i+1}$ is the approximation of $\mathbf{x}_r$ obtained in step $i+1$, then:

$$\mathbf{F}\left(\mathbf{x}_r^i\right) + \frac{\partial \mathbf{F}\left(\mathbf{x}_r^i\right)}{\partial \mathbf{x}}\left(\mathbf{x}_r^{i+1} - \mathbf{x}_r^i\right) = \mathbf{0} \tag{3}$$

and

$$\mathbf{x}_r^{i+1} = \mathbf{x}_r^i - \frac{\partial \mathbf{F}^{-1}\left(\mathbf{x}_r^i\right)}{\partial \mathbf{x}}\mathbf{F}\left(\mathbf{x}_r^i\right). \tag{4}$$

The Newton-Raphson procedure is repeated until $\left\|\mathbf{F}\left(\mathbf{x}_r^{i+1}\right)\right\| = 0.5$. This tolerance is enough to assure fast convergence.

Figure 5 contains the result for the example used in the previous section, with a total computing time of 3.6s.

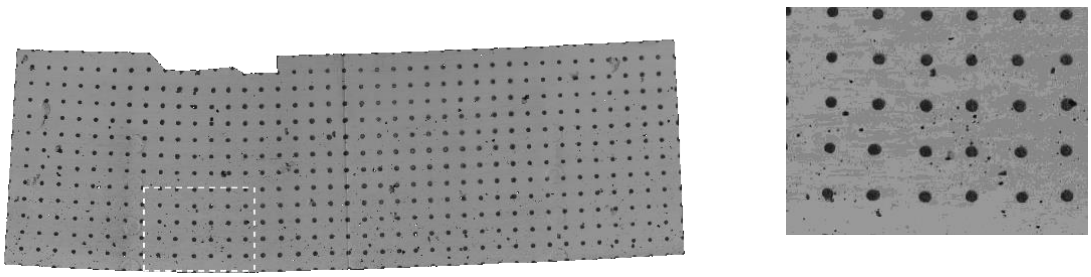

(a) (b)

Figure 5 – Inverse approach: (a) current virtual frame; and (b) detail of the virtual frame.

2.2.3. Simplified approach

As mentioned in Section 2.2, $\mathbf{u}_r$ is a function of the reference coordinates of the pixel. A simplified approach can be obtained if the displacement field is interpolated in the virtual frame with the set of scattered photogrammetric or image correlation points used to measure displacements. The displacement function, now symbolically written as $\mathbf{u}_r\left(\mathbf{x}_c\right)$, represents an interpolation of this data within the virtual frame. Although approximate, this procedure avoids solving the system of equations in the previous section, as the position of the pixel in the reference frame can be directly calculated from:

$$\mathbf{x}_r = \mathbf{x}_c - \mathbf{u}_r\left(\mathbf{x}_c\right) \tag{5}$$

and the corresponding image data is transferred to position $\mathbf{x}_c$ in the current virtual frame.

The total required time for computing the example from the previous sections was 2.3s and the result is similar to the one in Figure 5.

2.3. Identification of crack events

As discussed in Section 2.1, any change occurring between initial and current time frames can be characterised by directly computing the difference between virtual and real current frames. Figures 6a and 6b are the result after subtracting Figure 3a to Figure 5a (inverse colours have been used for clarity).

The resulting map can be superimposed with the real current frame to highlight all crack events, leading to Figures 6c and 6d. Note that the current real frame was made darker to increase contrast. Any initially existing discontinuity such as a crack, a shadow, a surface imperfection or even painted targets, are not misleadingly identified, because they appear in both virtual and real frames.

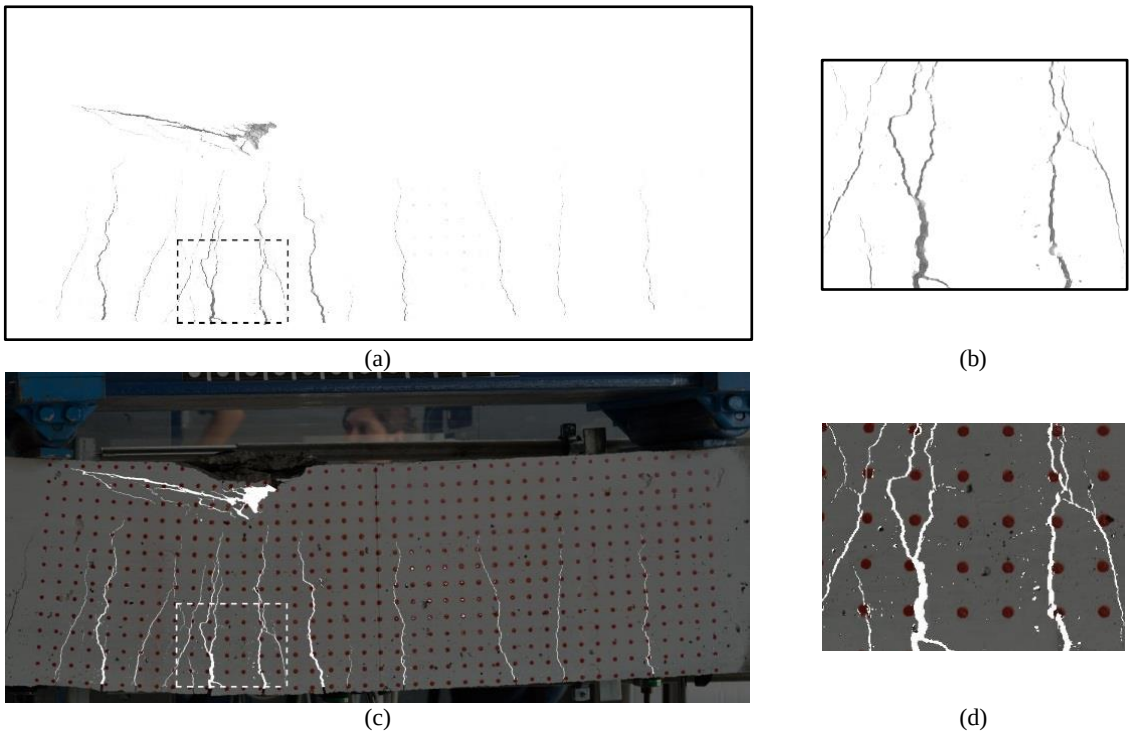

(a) (b)

(c) (d)

Figure 6 – Crack events: (a) difference between virtual and real current frames; (b) detail; (c) results superimposed with the current real frame; and (d) detail.

3. Case studies

This section contains two experimental tests to illustrate the method. For each experimental test, only the most relevant information is given. Sections 3.1.1 and 3.2.1, designated "Preliminary considerations",

contain all information related with each test procedure, including image acquisition, target detection and error assessment. All issues strictly related with the image deformation and its results are thoroughly presented in Sections 3.1.2 and 3.2.2, designated "Image Deformation Approach".

3.1. Lightweight high-strength concrete beam

This section describes a flexural test on a high-strength lightweight concrete beam with a density of 1870 kg/m^3 and a mean compressive strength of 51 MPa at 28 days of age. The structural scheme, load and boundary conditions are represented in Figure 7a. The cross-section of the beam is represented in Figure 7b, including the S500 steel reinforcement bars. More details can be found in [27].

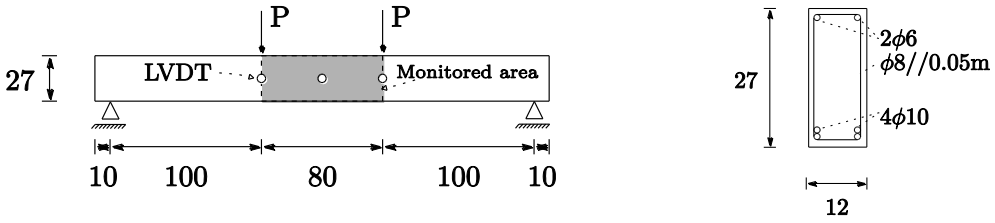

(a) (b)

Figure 7 – Lightweight high-strength concrete beam: (a) structural scheme, load and boundary conditions; and (b) cross-section (dimensions in cm)

The survey area is schematically represented in Figure 7a, whereas the corresponding image frames are shown in Figure 8 for all selected instants. These are also represented in the load vs. vertical displacement curve depicted in Figure 9a.

3.1.1. Preliminary considerations

No special attention was given to lighting conditions. A regular digital camera was installed on a tripod at approximately 180 cm from the surface of the specimen and triggered using a remote shutter. All images were acquired at maximum resolution, i.e., 4608×3072 pixel and 48-bit depth, using a 55 mm focal length lens.

The displacement field at the surface of the specimen was measured using photogrammetry [3-5]. For that purpose, circular targets with 5 mm diameter were painted with centres placed according to a regular grid of 20 mm. The Hough transform was used to detect the geometrical centre of all targets, for all defined stages (a complete description of the procedure can be found in Ballard [28]). In this first experimental test, the surface of the specimen was painted white for higher contrast.

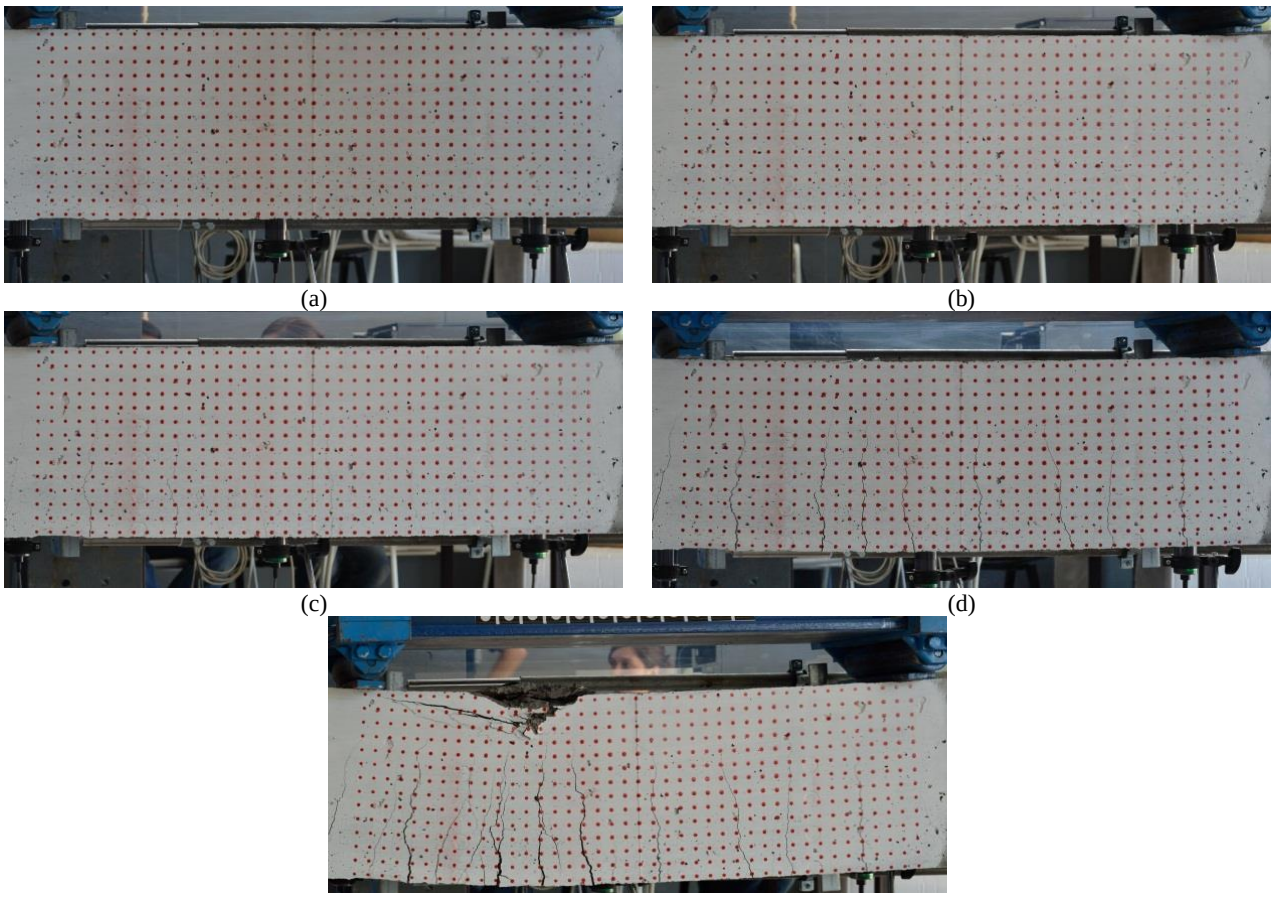

Figure 8 – Lightweight high-strength concrete beam: (a) stage 0; (b) stage 1; (c) stage 2; (d) stage 3; and (e) stage 4.

Immediately before starting the test, ten images were acquired within a short period of time. These images were later used to assess the target detection error and to scale and align all subsequent images using a homography (more details in [29-31]). The displacement field was computed at each stage by measuring the coordinates relatively to any selected reference frame.

The load vs. vertical displacement measured by LVDT at mid-span (see Figure 7a) is represented in Figure 9a. The displacement for the target closer to the LVDT is also represented in the same image for all stages. Figure 9b shows the high correlation between LVDTs and photogrammetry for the three control points (represented in Figure 7a) in all stages. This validates the displacement field measured by photogrammetry.

The ten images acquired at the beginning of the test allowed computing the error in the homography, which is measured by the difference between real target coordinates (defined by the known grid spacing) and the coordinates averaged from the image, and the root mean square precision from the differences found in each of the ten images for the coordinates of each target. The homography error was on average 0.177 mm, whereas the minimum and maximum values were, respectively, 0.068 mm and 0.806 mm. Since this is a

systematic error affecting the real coordinates of each pixel, it tends to vanish when computing relative displacements. Consequently, the error in the displacements is considered to be exclusively due to the target detection algorithm. This error was on average 0.037 mm, having a minimum of 0.013 mm and a maximum of 0.019 mm. Figures 10a and 10b show the representation of both errors along x- and y-axes.

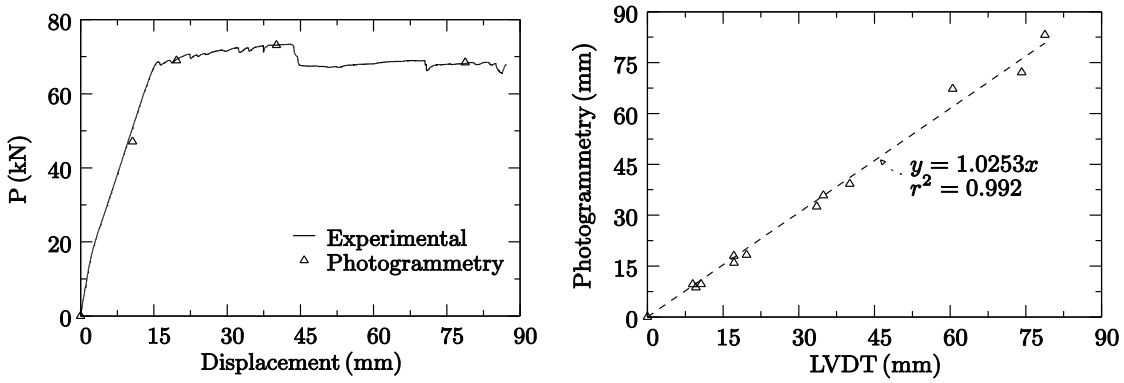

(a) (b)

Figure 9 – Lightweight high-strength concrete beam: (a) load vs. vertical displacement; (b) Photogrammetry vs. LVDT.

Finally, all images were aligned and scaled to 1:4 using the homographic parameters, since the mean resolution of the original image frames was circa 0.25mm/pixel.

The displacement field at the surface was linearly interpolated by means of a Delaunay triangular mesh using all available targets.

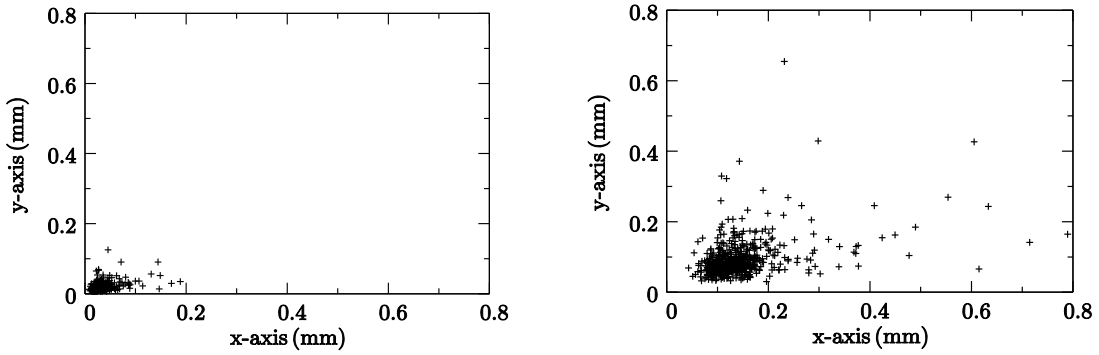

(a) (b)

Figure 10 – Lightweight high-strength concrete beam: (a) precision; and (b) error in the homography along x- and y-axes.

3.1.2. Image Deformation Approach

The procedure is herein applied using the simplified approach discussed in Section 2.2.3 and stage 0 the reference frame (Figure 8a) for subsequent stages (Figures 8b to 8e). As discussed in Section 2.3, the difference between virtual and current real frames was computed and superimposed to the real current frame. All results are represented in Figures 11 to 13.

Cracks initially appearing in stage 1 are barely noticeable in Figure 11a. Nevertheless, the image deformation approach was capable of detecting discontinuities above 1 pixel width (compare Figures 12a and 12b, or Figures 13a and 13b). Furthermore, it appears insensitive to pre-existing imperfections at the surface, such as the vertical line clearly seen in the specimen (e.g. Figure 11a) or even the painted targets, which vanish in the analysis.

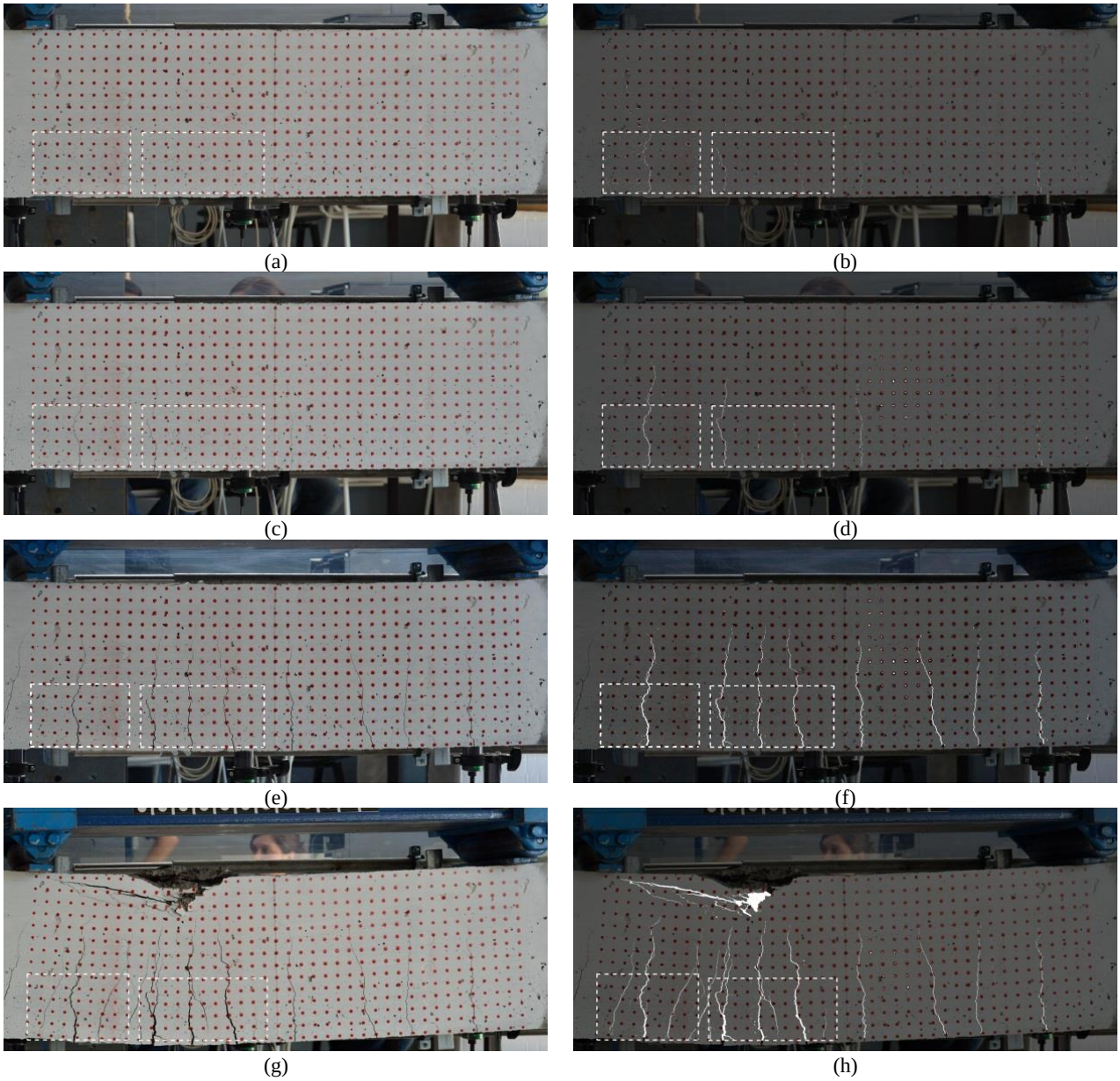

Figure 11 – Lightweight high-strength concrete beam – real current frame and crack events (highlighted in white), respectively: (a) and (b) stage 1; (c) and (d) stage 2; (e) and (f) stage 3; (g) and (h) stage 4.

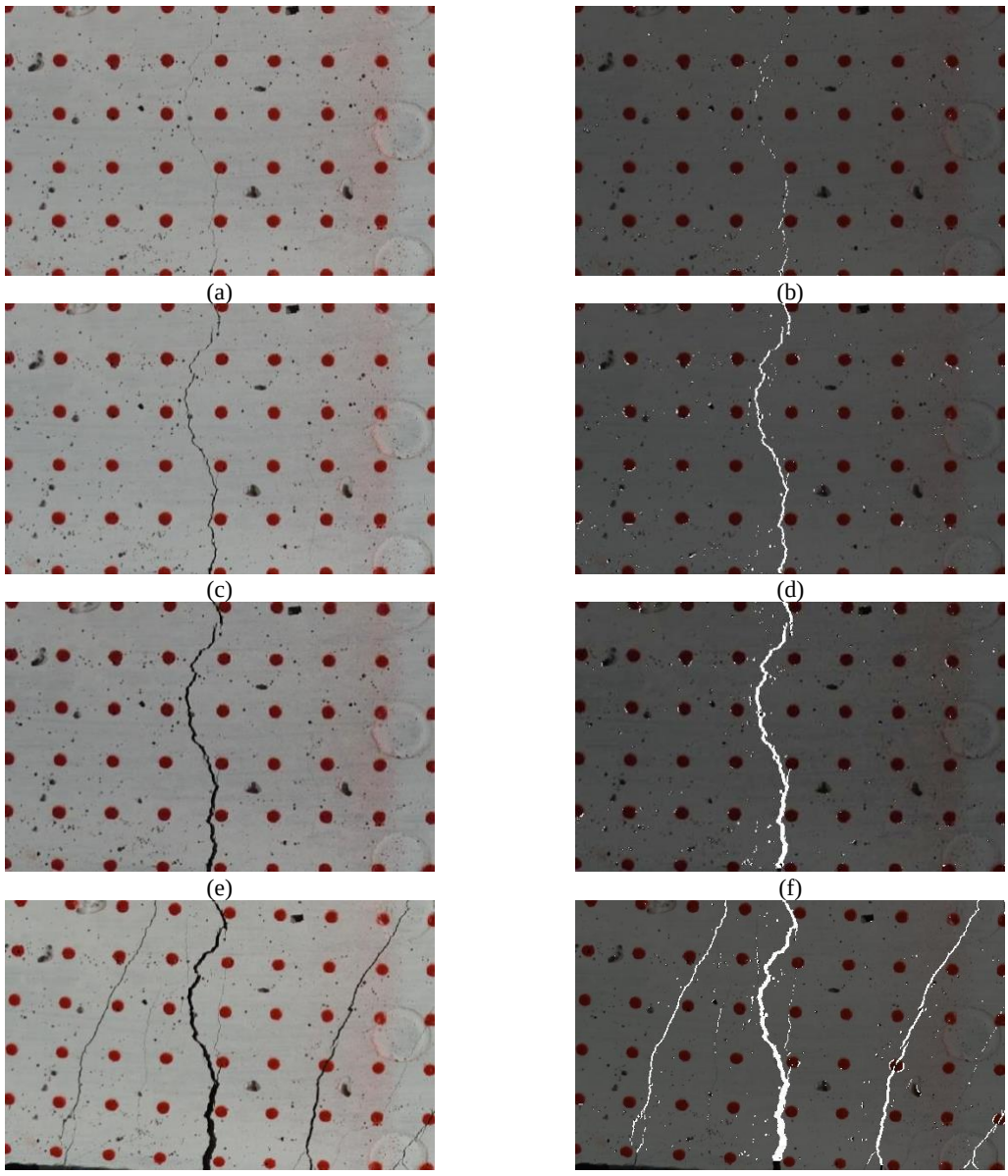

Figure 12 – Lightweight high-strength concrete beam – left region of interest in the real current frame and corresponding crack events (highlighted in white), respectively: (a) and (b) stage 1; (c) and (d) stage 2; (e) and (f) stage 3; (g) and (h) stage 4.

The method is now applied to stage 4 (Figure 8e) assuming stage 3 (Figure 8d) as reference. This procedure allows monitoring any 'non-smooth' event occurring between those two stages. Results are represented in Figures 14 to 16. Between the two monitored stages, the cracks on the right side of the specimen remain practically unchanged – see Figures 14a and 14b. For this reason, Figure **Error! Reference source not found.**c does not highlight any crack in that region.

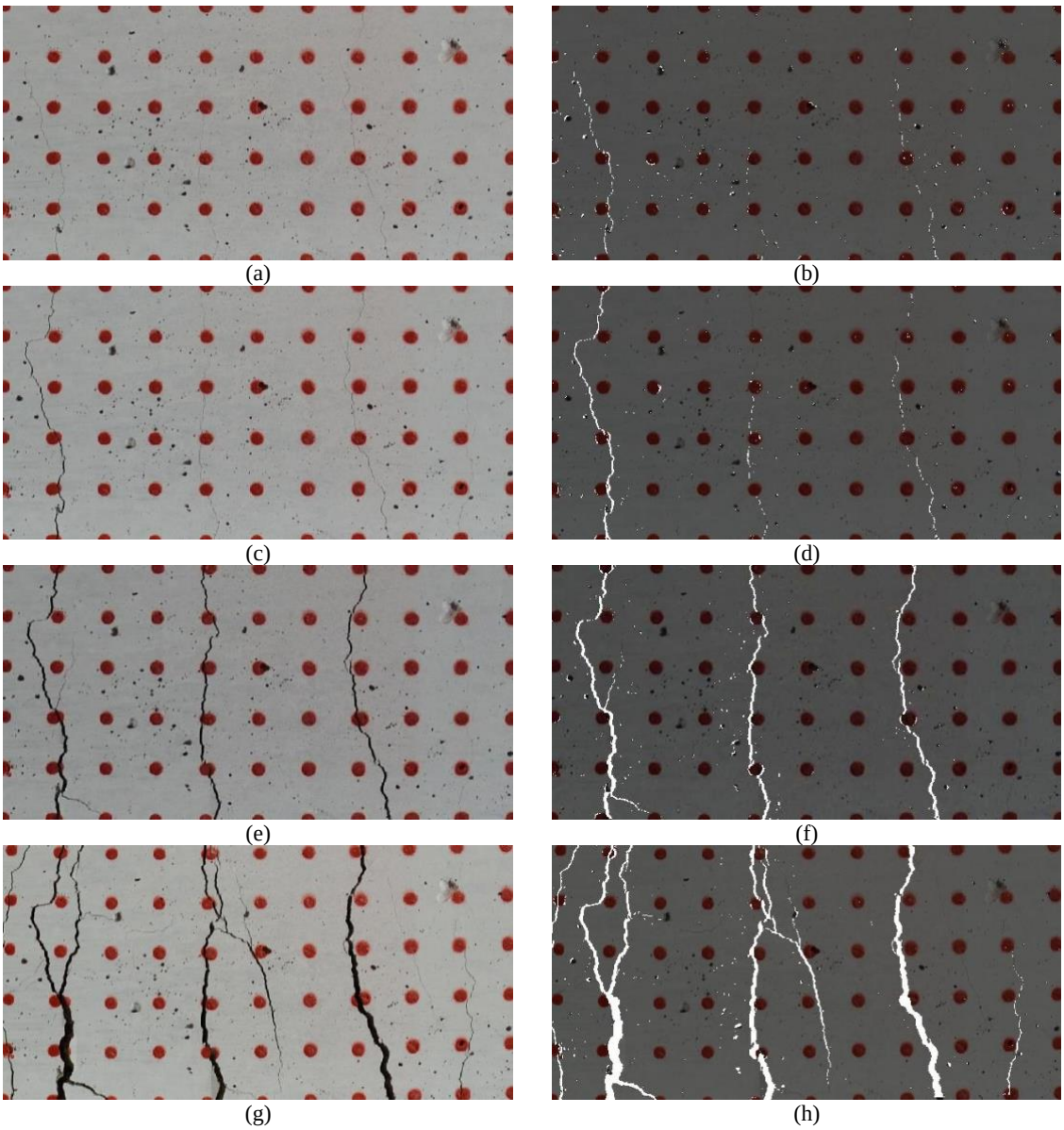

Figure 13 – Lightweight high-strength concrete beam – right region of interest in the real current frame and corresponding crack events (highlighted in white), respectively: (a) and (b) stage 1; (c) and (d) stage 2; (e) and (f) stage 3; (g) and (h) stage 4.

The two regions of interest marked in Figure 14 are represented in Figures 15 and 16. From these Figures, the discontinuous changes between the two selected stages of analysis can be identified by the image deformation approach. For instance, for the crack represented in Figure 15b at the middle, only the left edge opened between stages 3 and 4, being the right edge almost unchanged. The right crack in Figure 16b opened practically symmetrically in the lower part, whereas the edge is the one opening at the middle and upper regions of interest. Up to the authors' knowledge, this is the only existing approach capable of performing such analysis. Visually, these changes are nearly impossible to detect.

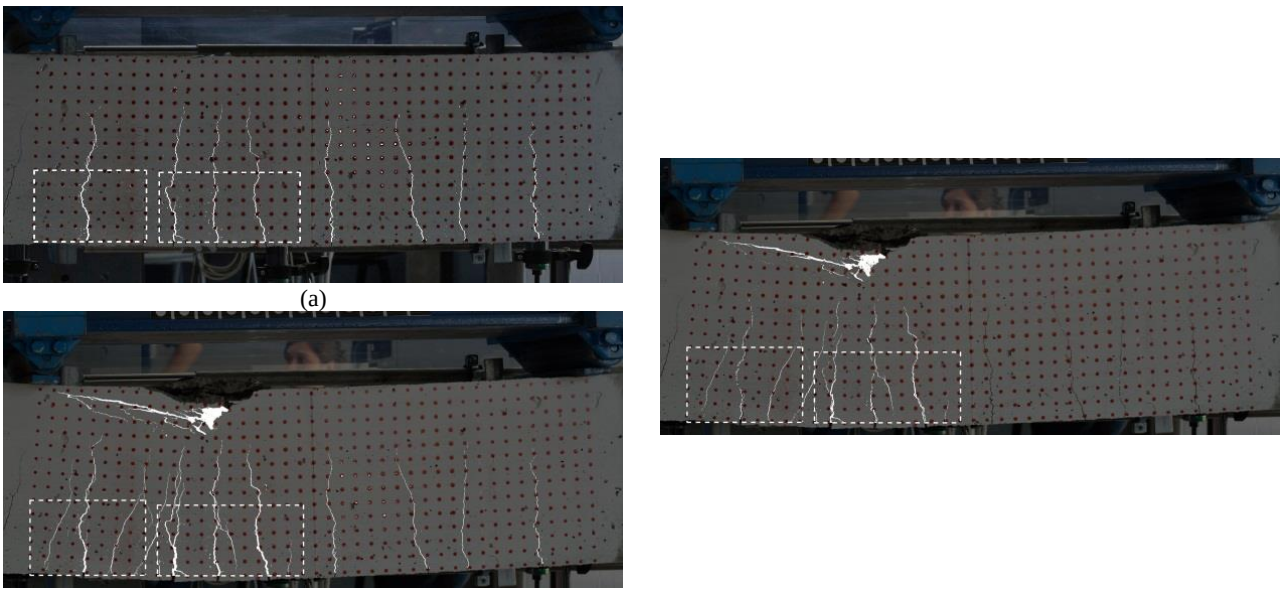

(a) (b) (c)

Figure 14 – Lightweight high-strength concrete beam – crack events (highlighted in white) in: stages 3 and 4, respectively (a) and (b), taking stage 0 as reference; and (c) stage 4, taking stage 3 as reference.

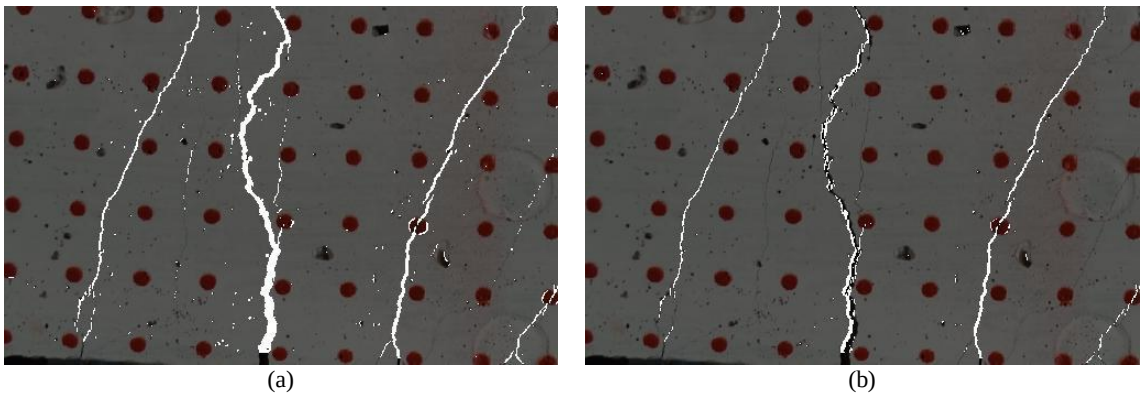

(a) (b)

Figure 15 – Lightweight high-strength concrete beam – crack events (highlighted in white) in the left region of interest in stage 4, taking: (a) stage 0; and (b) stage 3, as reference.

Finally, since the obtained frames are scaled 1:4, any measurement related with the geometry of cracks (e.g. crack width, length, area or path) can be obtained for any stage of loading (see for instance [32]).

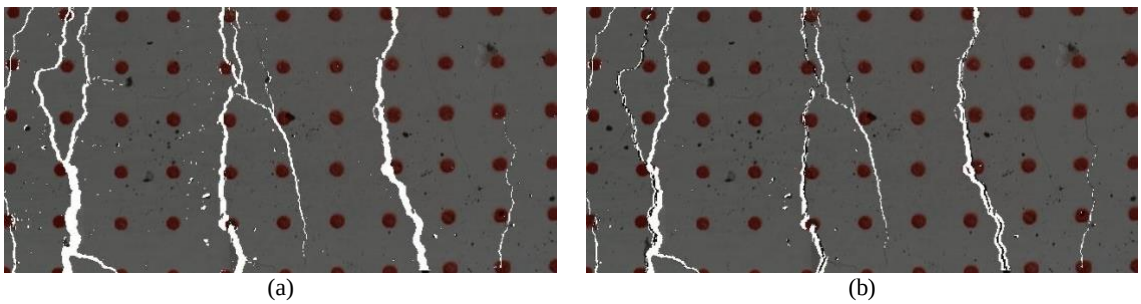

(a) (b)

Figure 16 – Lightweight high-strength concrete beam – 'non-smooth' events (highlighted in white) in the right region of interest in stage 4, taking: (a) stage 0; and (b) stage 3, as reference.

3.2. High strength concrete beam

This section describes the application to a shear test performed on a high-strength prestressed concrete (HSC) beam. The corresponding structural scheme, load and boundary conditions are represented in Figure 17a.

The cross-section of the beam was 'I'-shaped with 50 cm height, the bottom flange was 30 cm wide with thickness ranging from 7.5 to 10.0 cm, whereas the upper flange, also 30 cm wide, had a thickness varying between 6.0 to 6.5 cm (see Figure 17b). Twelve adherent strands were placed at the bottom flange, whereas the upper flange contains two non-adherent strands. The prestress was released at the age of 7 days, whereas the experimental shear test was performed at 6 years of age. The HSC presented an average compressive strength of 120 MPa at 28 days of age [33].

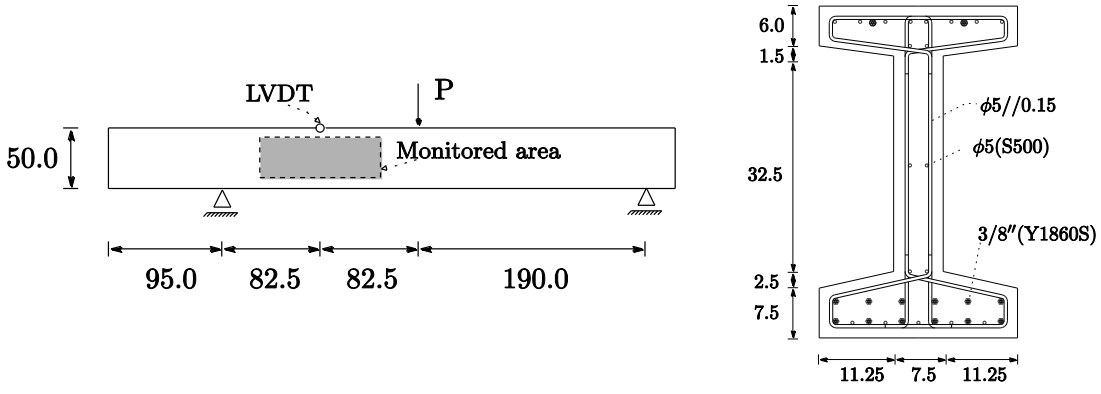

(a) (b)

Figure 17 – Prestressed HSC beam: structural scheme, load and boundary conditions; and (b) cross-section (dimensions in cm)

Figure 18 shows the surveying area identified in Figure 17a for all monitored instants. These are also represented in the load vs. vertical displacement curve in Figure 19a.

This test has been selected due to the poorly treated surface, which presented several initial imperfections (see Figure 18). Therefore, this is a demanding test regarding the robustness of the approach.

3.2.1. Preliminary considerations

The procedure adopted is the same as described in Section 3.1.1. For this reason, only the main aspects and differences are mentioned herein. In this case, the camera was installed at approximately 90 cm from the surface of the specimen and images were acquired at maximum resolution, i.e., 4608×3072 pixel and 48-bit depth, using a 55 mm focal length lens. The diameter of each target painted at the surface was 10 mm and the centres defined a grid with 25 mm spacing – see Figure 18.

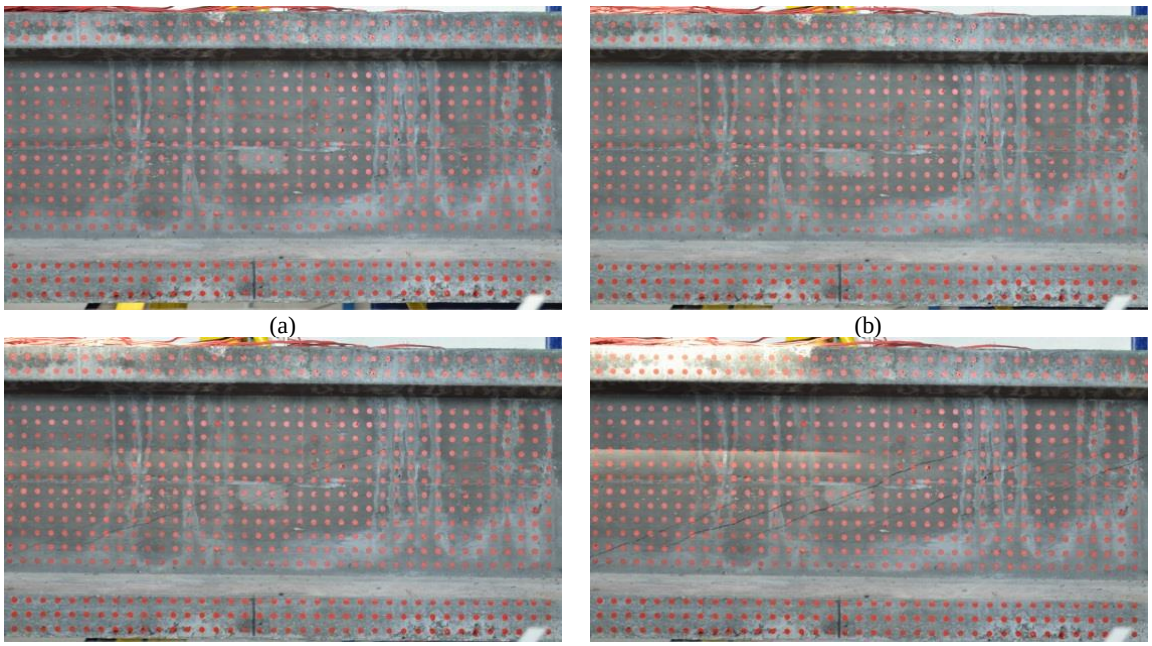

(a) (b) (c) (d)

Figure 18 – Prestressed HSC beam: (a) stage 0; (b) stage 1; (c) stage 2; and (d) stage 3.

Figure 19a presents the load vs. displacement at the target nearer to the LVDT (see Figure 17a), whereas Figure 19b shows the high correlation between the two.

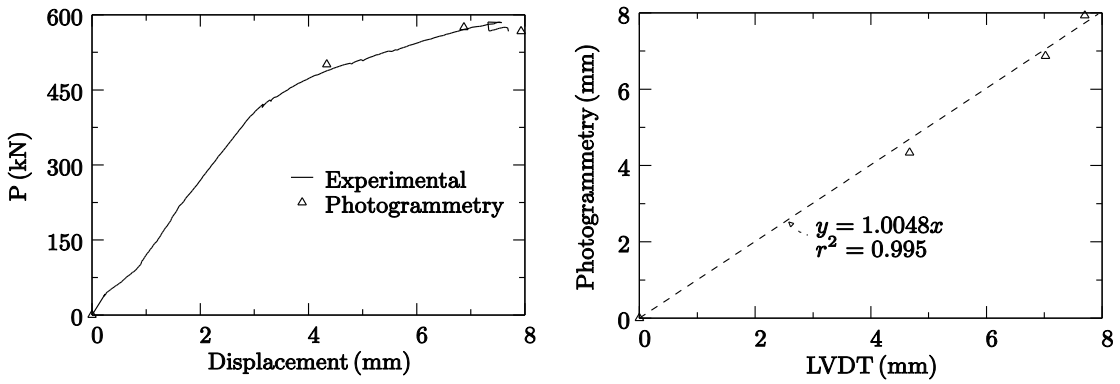

(a) (b)

Figure 19 – Prestressed HSC beam: (a) load vs. vertical displacement; (b) photogrammetry vs. LVDT.

The homography error and precision are represented in Figure 20. In this case, the homography error was on average 0.162 mm, whereas the minimum and maximum values were, respectively, 0.086 mm and 0.293 mm. The precision was on average 0.042 mm, having a minimum of 0.022 mm and a maximum of 0.075 mm.

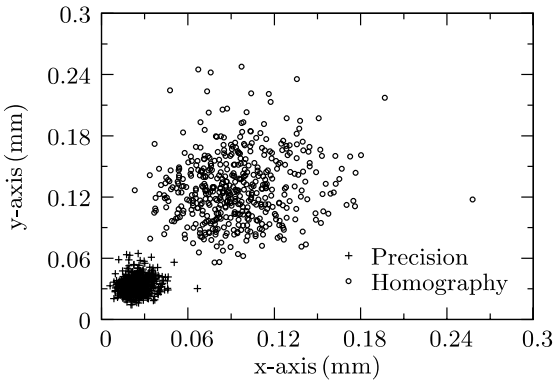

Figure 20 – Prestressed HSC beam: error in the homography and precision along x- and y-axes.

3.2.2. Image Deformation Approach

Following the same procedure presented in Section 3.1.2, results are represented in Figures 21 to 23. Figure 21 compares the real current frame and the 'non-smooth' events detected when subtracting the real from the virtual current frames. Two selected areas, both on the left and right sides of the monitored area, are magnified and shown in Figures 22 and 23. These areas are identified in Figure 21 using dashed lines.

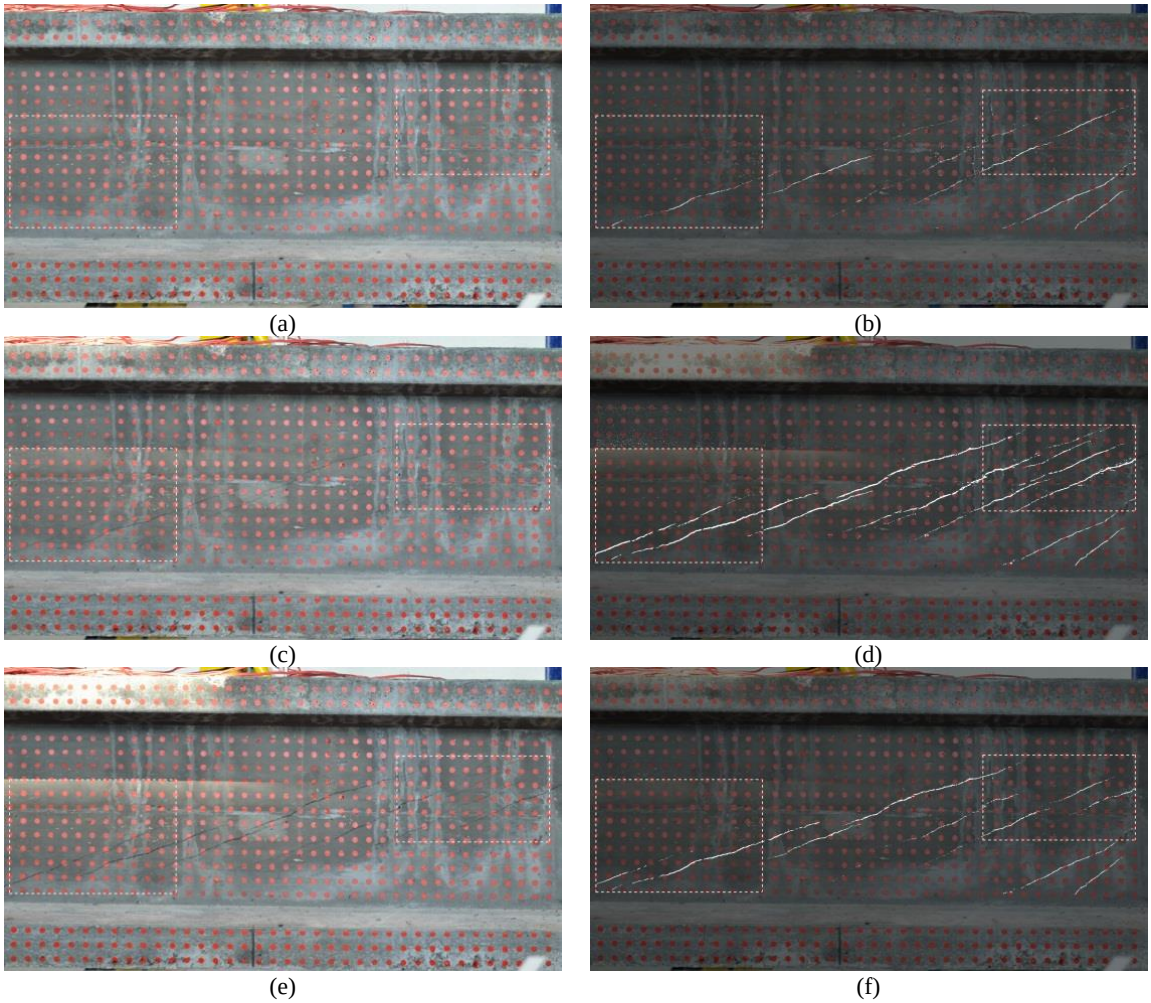

Figure 21 – Prestressed HSC beam – real current frame and frame containing the crack events (highlighted in white), respectively: (a) and (b) stage 1; (c) and (d) stage 2; (e) and (f) stage 3.

Similarly to what was already observed in Section 3.1.2, the image deformation approach allows detecting initial cracks slightly above 1 pixel width already in stage 1. These cracks are very hard to identify visually (see Figure 21a and compare Figures 22a and 22b, or Figures 23a and 23b).

The main conclusion to retain is the fact of the approach being practically insensitive to shadows created by gradually varying lighting conditions (e.g. a shadow appears in Figure 21c, but not in Figure 21f) and, more importantly, to any surface imperfection such as stains, voids or small damages initially present at the surface of the specimen. This means that the approach is particularly robust and does not require any specific preparation of the surface.

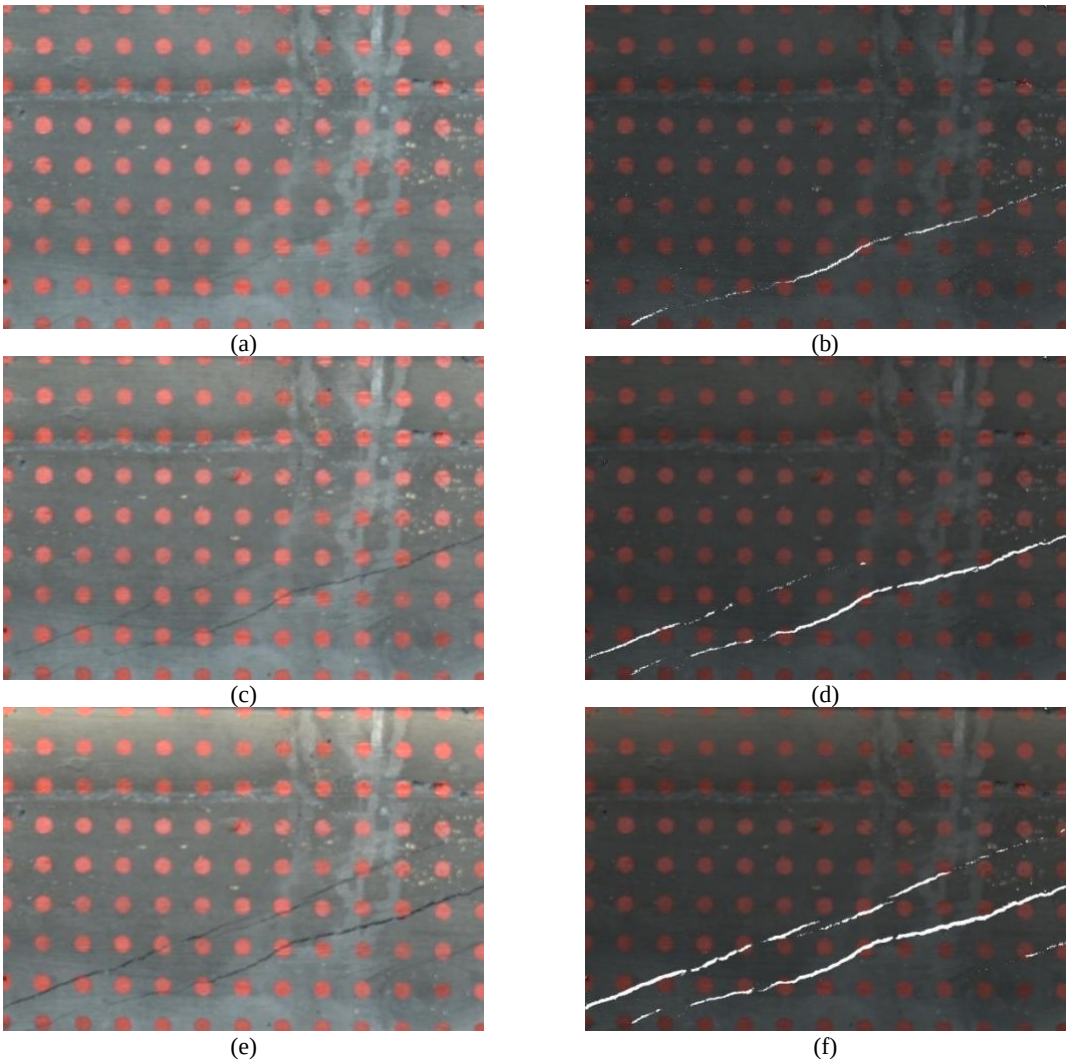

Figure 22 – Prestressed HSC beam – detail on the left of the real current frame and the frame containing the crack events (highlighted in white), respectively: (a) and (b) stage 1; (c) and (d) stage 2; (e) and (f) stage 3.

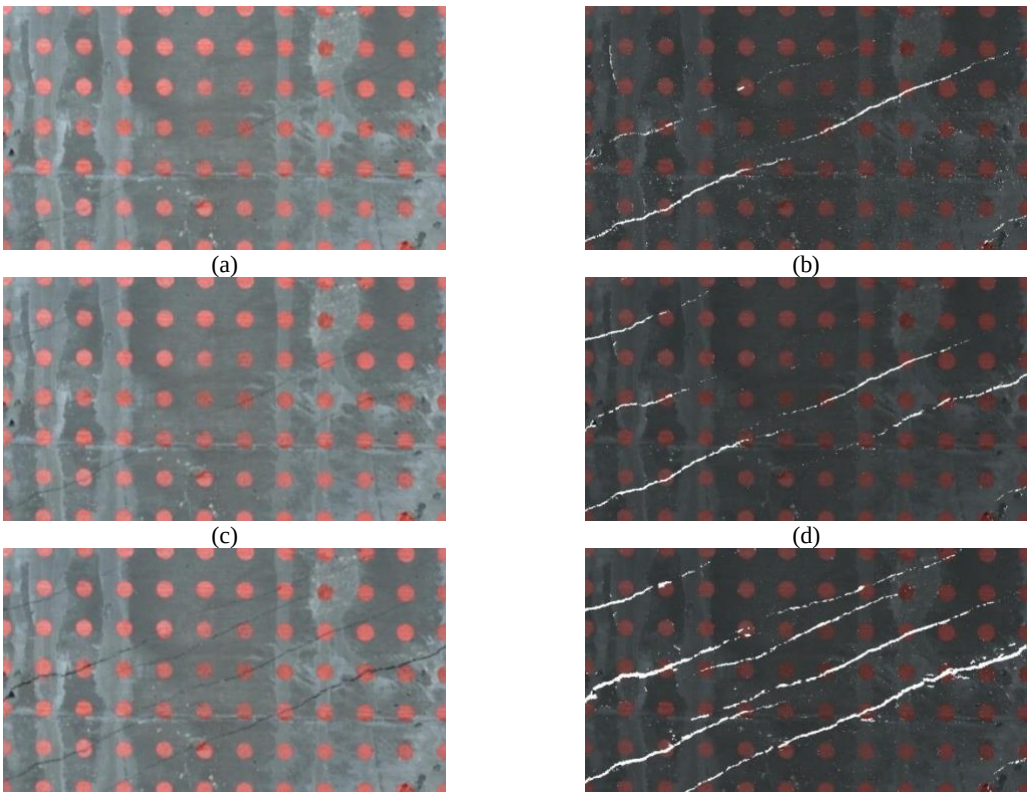

Figure 23 – Prestressed HSC beam – detail on the right of the real current frame and the frame containing the 'non-smooth' events (highlighted in white), respectively: (a) and (b) stage 1; (c) and (d) stage 2; (e) and (f) stage 3.

4. Conclusions

In the scope of structural health monitoring, surface cracks are still frequently mapped by sketches based on visual observations, being the crack openings evaluated by means of measuring magnifiers or crack width rulers. This rather empirical process is time-consuming and prone to human errors. Furthermore, it is very difficult to monitor crack propagation and evolution through time.

Different procedures have recently been proposed to overcome, or at least mitigate, the above-mentioned drawbacks. Nevertheless, in spite of the technological developments, nearly all procedures present limitations in what concerns monitoring crack propagation within a time interval. Typically, the crack pattern is depicted for each time instant independently from any previous history and is not possible to accurately identify changes occurring within a given time interval. Most existing techniques can only be applied in very simple tests, under strictly controlled conditions regarding surface and lighting conditions, mainly to avoid false detections.

A different monitoring strategy is followed in this manuscript, which is based on an image deformation approach. With this approach, an initial reference image is deformed to match a given stage of analysis using

the real displacements provided by photogrammetry or image correlation. Both deformed (virtual) image and current real images should match, except if new crack events happened since acquiring the reference picture. These changes include new cracks, crack propagation and openings, and can be straightforwardly identified by comparing both virtual and real frames.

The approach was applied to monitoring crack propagation in concrete members, herein used as case studies. Following this study, it could be observed that the approach is computationally efficient, requires reduced computational time and is insensitive to any discontinuity previously existing at the surface, such as cracks, stains, voids or shadows. No special lighting conditions are required to enhance results and the process of crack propagation. In fact, the crack opening/closure occurring within selected time interval can be adequately characterised without specific surface treatments to enhance detection. Finally, it should also be mentioned that the approach can provide good results in relatively large surveying areas and is not constrained to concrete cracks. Similar procedure can be applied to different materials with the purpose of detecting and characterising multiple sources of surface discontinuities within the range of the camera resolution.

5. Acknowledgements

The authors would also like to extend their acknowledgement to the support provided by FEDER funds through the Operational Programme for Competitiveness Factors – COMPETE – by Portuguese funds through FCT – Portuguese Foundation for Science and Technology under Project No. FCOMP-01-0124-FEDER-020275 (FCT ref. PTDC/ECM/119214/2010). D. Dias-da-Costa would like to acknowledge the support from the Australian Research Council through its Discovery Early Career Researcher Award (DE150101703) and from the Faculty of Engineering & Information Technologies, The University of Sydney, under the Faculty Research Cluster Program. J. Valença also extends his acknowledgement to the financial support of the Portuguese Foundation for Science and Technology, post-doctoral grant FCT ref. SFRH/BPD/102790/ 2014.

References

1. Yao, Y., S.-T.E. Tung, and B. Glisic, *Crack detection and characterization techniques—An overview.* Structural Control and Health Monitoring, 2014. **21**(12): p. 1387-1413.
2. Yin, Z., C. Wu, and G. Chen, *Concrete crack detection through full-field displacement and curvature measurements by visual mark tracking: A proof-of-concept study*. Structural Health Monitoring, 2014. **13**(2): p. 205-218.
3. Lange, J., W. Benning, and K. Siering. *Crack detection at concrete construction units from photogrammetric data using image processing procedures*. in *ISPRS Commission VII Mid-term Symposium Remote Sensing: From Pixels to Processes*. 2006. Enschede, Netherlands.
4. Dias-da-Costa, D., J. Valença, and E. Júlio, *Laboratorial test monitoring applying photogrammetric post-processing procedures to surface displacements.* Measurement, 2011. **44**(3): p. 527-538.
5. Hegger, J., A. Sherif, and S. Görtz, *Investigation of pre-and postcracking shear behavior of prestressed concrete beams using innovative measuring techniques.* ACI Structural Journal, 2004. **101**(2): p. 183-192.
6. McCarthy, D.M.J., J.H. Chandler, and A. Palmeri, *Monitoring Dynamic Structural Tests Using Image Deblurring Techniques.* Key Engineering Materials, 2013. **569-570**: p. 932-939.
7. Lecompte, D., J. Vantomme, and H. Sol, *Crack Detection in a Concrete Beam using Two Different Camera Techniques.* Structural Health Monitoring, 2006. **5**(1): p. 59-68.
8. Tung, S., S. M., and W. Sung, *Development of digital image correlation method to analyse crack variations of masonry wall.* Sadhana, 2008. **33**(6): p. 767-779.
9. Shah, S. and J. Chandra Kishen, *Fracture Properties of Concrete–Concrete Interfaces Using Digital Image Correlation.* Experimental Mechanics, 2011. **51**(3): p. 303-313.
10. Hoffman, M.E., et al., *Computing strain fields from discrete displacement fields in 2D-solids.* International Journal of Solids and Structures, 1996. **33**(29): p. 4293-4307.
11. Chen, H. and R. Leung Su, *Study on fracture behaviors of concrete using electronic speckle pattern interferometry and finite element method.* ICCES, 2010. **15**(3): p. 91-101.
12. Wen, T.-K. and C.-C. Yin, *Crack detection in photovoltaic cells by interferometric analysis of electronic speckle patterns.* Solar Energy Materials and Solar Cells, 2012. **98**(0): p. 216-223.
13. Rossi, M., F. Pierron, and P. Forquin, *Assessment of the metrological performance of an in situ storage image sensor ultra-high speed camera for full-field deformation measurements.* Measurement Science and Technology, 2014. **25**(2): p. 025401.
14. De Wilder, K., et al., *Experimental investigation on the shear capacity of prestressed concrete beams using digital image correlation.* Engineering Structures, 2015. **82**(0): p. 82-92.
15. Abdel-Quarter, I., O. Abudayyeh, and M. Kelly, *Analysis of edge detection techniques for crack identification in bridges.* Journal of Computing in Civil Engineering, 2003. **17**(3): p. 255-263.
16. Valença, J., D. Dias-da-Costa, and E.N.B.S. Júlio, *Characterisation of concrete cracking during laboratorial tests using image processing.* Construction and Building Materials, 2012. **28**(1): p. 607-615.
17. Rodríguez-Martin, M., et al., *Cooling analysis of welded materials for crack detection using infrared thermography*. Infrared Physics & Technology, 2014. **67**(0): p. 547-554.
18. Subirats, P., et al. *Automation of Pavement Surface Crack Detection using the Continuous Wavelet Transform*. in *Image Processing, 2006 IEEE International Conference on*. 2006.
19. Sohn, H.-G., et al., *Monitoring crack changes in concrete structures.* Computer-Aided Civil and Infrastructure Engineering, 2005. **20**(1): p. 52-61.
20. Yamaguchi, T., et al., *Image-based crack detection for real concrete surfaces.* IEEJ Transactions on Electrical and Electronic Engineering, 2008. **3**(1): p. 128-135.
21. Valença, J., et al., *Automatic concrete health monitoring: assessment and monitoring of concrete surfaces.* Structure and Infrastructure Engineering, 2014. **10**(12): p. 1547-1554.
22. Valença, J., et al., *Automatic crack monitoring using photogrammetry and image processing.* Measurement, 2013. **46**(1): p. 433-441.
23. Bray, J., et al. *A Neural Network based Technique for Automatic Classification of Road Cracks*. in *Neural Networks, 2006. IJCNN '06. International Joint Conference on*. 2006.
24. Zienkiewicz, O.C. and J.Z. Zhu, *The superconvergent patch recovery and a posteriori error estimates. Part 1: The recovery technique.* International Journal for Numerical Methods in Engineering, 1992. **33**(7): p. 1331-1364.

25. Bookstein, F.L., *Principal warps: thin-plate splines and the decomposition of deformations.* IEEE Transactions Pattern Analysis and Machine Intelligence 1989. **11**: p. 567-585.
26. Godinho, L., et al., *An efficient technique for surface strain recovery from photogrammetric data using meshless interpolation.* Strain, 2013. **50**: p. 132-146.
27. Carmo, R.N.F., et al., *Influence of both concrete strength and transverse confinement on bending behavior of reinforced LWAC beams.* Engineering Structures, 2013. **48**: p. 329-341.
28. Ballard, D., *Generalizing the Hough Transform to Find Arbitrary Shapes.* Pattern Recognition, 1981. **13**: p. 111–122.
29. Criminisi, A., I. Reid, and A. Zisserman, *Single view metrology*. Int. J. Comput. Vision, 2000. **40**(2): p. 123-148.
30. Hartley, R. and A. Zisserman, *Multiple view geomerty in computer vision*. second edition ed. 2003, Cambridge: Cambridge University Press.
31. Dworakowski, Z., et al., *Vision-based algorithms for damage detection and localization in structural health monitoring.* Structural Control and Health Monitoring, 2016. **23**(1): p. 35-50.
32. Barazzetti, L. and M. Scaioni, *Crack measurement: development, testing and applications of an automatic image-based algorithm.* ISPRS Journal of Photogrammetry and Remote Sensing, 2009. **64**(3): p. 285-296.
33. Fernandes, P., *Long Span High Strength Concrete Beams - Viability, Design, Production and Behaviour*, in *Department of Civil Engineering*2007 (*in Portuguese*), University of Coimbra: Coimbra.